Mechanism of secondary eyewall formation in tropical cyclones revealed by sensitivity experiments on the mesoscale descending inflow

Kyohei Kasami[1], Masaki Satoh[1,2]

[1] *Atmosphere and Ocean Research Institute, The University of Tokyo, Kashiwa, Japan*

[2] *Typhoon Science and Technology Research Center, Yokohama National University, Yokohama, Japan*

Corresponding author: Masaki Satoh, Atmosphere and Ocean Research Institute, The University of Tokyo, 5-1-5 Kashiwanoha, Kashiwa, 277-8564, Japan. E-mail: satoh@aori.u-tokyo.ac.jp

Submitted to SOLA

June 6, 2023

Abstract

An eyewall replacement cycle is often seen in tropical cyclones, when a secondary eyewall forms outside the inner eyewall, and the inner eyewall disappears. Although this cycle significantly affects the intensity of tropical cyclones, the mechanisms of secondary eyewall formation (SEF) are unclear. Some studies have suggested that dry air inflow and diabatic cooling may have an important role in SEF via the mesoscale descending inflow (MDI). Here, we use numerical experiments to investigate the role of the middle and

upper tropospheric dry inflow in SEF. Idealized experiments were conducted using the plane version of the nonhydrostatic icosahedral atmospheric model. Control experiments produced SEF with a dry air inflow in the middle and upper troposphere and associated MDI. In sensitivity experiments, in which the water vapor in the middle and upper troposphere was increased in the outer areas of the tropical cyclone, SEF was hindered and slowed down. These results reveal the role of the dry inflow and associated MDI in SEF.

1. Introduction

Eyewall replacement occurs when a secondary eyewall forms outside the inner eyewall of a tropical cyclone (TC), and the inner eyewall disappear. Although many studies have investigated concentric eyewalls and eyewall replacement cycles, there is still no consensus on the mechanism of secondary eyewall formation (SEF). Proposed mechanisms include axisymmetrization of vorticity anomalies (Terwey and Montgomery 2008), frictional upwelling due to localized increases in vorticity gradients (Kepert 2013), boundary-layer non-equilibrium dynamics (Huang et al. 2012), and lower-level heating of rainbands (Zhu and Zhu 2014). Huang et al. (2012) also highlight the importance of agradient wind in the boundary layer. In the boundary layer, angular momentum is transported inward of the TC by the inflow. The tangential wind speed increases when the inflow is enhanced, and the tendency due to angular momentum transport becomes larger than the frictional damping.

Recent studies have pointed to the role of the mid-troposphere inflow in SEF. Didlake et al. (2018) show that the mesoscale descending inflow (MDI) contributes to convective

enhancement and angular momentum transport in the SEF region. MDI is formed by diabatic cooling in stratiform precipitation regions (Didlake and Houze 2013). Kanada and Nishii (2023) use an observational study to suggest the importance of MDI in SEF. Ge (2015) investigated the effect of the water vapor field around typhoons on SEF, concluding that higher water vapor content favors SEF, which they attribute to the enhanced convective activity associated with the moistening of the atmosphere. However, Ge (2015) did not address the role of the water vapor field in the middle and upper troposphere in SEF. The detailed processes by which the middle and upper inflow influences SEF are not well understood.

In this study, we investigate the role of the dry air inflow and MDI using sensitivity experiments in an idealized setting. The paper is organized as follows. Section 2 presents the methodology, and Section 3 presents the results. Section 4 examines the mechanism of SEF by comparing the results with sensitivity experiments in which the amount of water vapor outside a TC varies. Section 5 provides a summary and a discussion of future considerations.

2. Methods

We used the plane version of the Nonhydrostatic ICosahedral Atmospheric Model (NICAM; Tomita and Satoh 2004; Satoh et al. 2008, 2014) to conduct an idealized experiment of a TC over the f-plane. NICAM is a global model composed of an icosahedral grid system, but in this experiment, we used a setup called plane-NICAM (Ohno and Satoh 2015; Satoh et al. 2014) in which a rhombic region corresponding to the two adjacent faces of the icosahedron is placed on a plane. When the periodic boundary

condition is imposed, this rhombic region is equivalent to a regular hexagonal region. In this study, we performed calculations for a rhombus of 4096 km per side, corresponding to a regular hexagon of 2365 km per side, with a horizontal grid spacing of 2 km, 74 vertical layers, and Coriolis parameters fixed at 20°N.

We used the Mellor-Yamada-Nakanishi-Niino scheme (Level 2) (Nakanishi, 2001; Nakanishi and Niino, 2004, 2006) for the boundary layer scheme, the NICAM Single-moment Water 6 model (NSW6; Tomita 2008; Roh and Satoh 2014) for the cloud microphysics scheme, and no convection scheme.

The vertical profiles of uniform horizontal temperature, pressure, and relative humidity were averaged from a one-month radiative-convective equilibrium experiment. In addition, an initial vortex was placed at the center of the domain. The shape of the initial vortex follows Rotunno and Emanuel (1987), and the parameters follow Wang et al. (2019); the vortex radius is 1000 km, the radius of maximum wind is 80 km, and the maximum wind speed is 25 m s^{-1}. Experiments in which no changes were made to the restart file were considered the control experiment (CTL).

After 108 h of integration of CTL, the sensitivity experiment was conducted by changing the water vapor mixing ratio outside the regular hexagonal region, which was centered on the center of the calculation domain. The inner domain, where the vapor mixing ratio was kept unchanged, is inside a regular hexagonal region with sides of length 384 km. We conducted two sensitivity experiments: one in which the water vapor mixing ratio was increased by 1.1 (qv1.1) between 6.0 km and 10.0 km in altitude and one in which it was increased by 1.2 (qv1.2). After changing the water vapor mixing ratio, the integration was performed for an additional 60 h.

3. Experiments and results

3.1. Control experiment (CTL)

Figure 1 shows the 1-h accumulated precipitation distribution at an integration time of 114 h to 144 h from the initial condition. (Hereafter, all integration times refer to the hours after the initial condition. At 114 h, eyewall clouds with precipitation of 40 mm or more are produced around the TC at a distance of 50 km from the center. Outside the eyewall, rainband precipitation areas are located around 200 km to 300 km from the TC center. At 120 h, rainband precipitation intensifies around the TC at a radius of 200 km. At 132 h, the precipitation area becomes axisymmetric at a radius of around 150 km, and an outer eyewall forms. At 144 h, the inner wall cloud almost completely disappears, indicating that the eyewall replacement has been achieved.

From this point forth, we focus mainly on the axisymmetric field. The radius-time cross-section of precipitation (Fig. 2(a)) shows the characteristics of the eyewall replacement: precipitation begins to intensify around the TC center at a radius of 300 km at 108 h. This precipitation intensifies and moves inward over time; from about 126 h, it intensifies rapidly and develops into the outer eyewall. At 144 h, precipitation at a radius of around 50 km weakens rapidly, and the inner eyewall disappears. The radius-time cross-section of the ground tangential wind speed (Fig. 2(b)) shows the same characteristics as the precipitation. At around 132 h, the radius of maximum tangential wind increases from the radius of the inner eyewall to that of the outer eyewall (Fig. 2(b)). Then, the outer eyewall gradually moves toward the TC center. Figure 2(c) shows time sequences of the maximum tangential wind and its radius. The speed of the maximum tangential wind decreases from around 100 h until 132 h and then increases. At that time, the radius of the maximum tangential wind jumps from about 50 km to about 130 km;

this indicates the eyewall replacement.

Next, we investigate the cross-section of the axisymmetric mean wind field at 114 h. At this time, the outer eyewalls are forming, which is considered representative of SEF. Fig. 3(a) shows that tangential wind reaches a maximum at a radius of around 50 km in the lower troposphere. This radius corresponds to the inner eyewall. In addition, a region of tangential wind speed greater than 35 m s^{-1} stretches from a radius of 350 km in the lower atmosphere to a radius of 250 km at an altitude of 8 km. This region corresponds to the inflow from the middle and upper troposphere in the radial wind field (Fig. 3(b)). Fig. 3(b) shows a strong inflow in the lowest layer of the atmosphere and a strong outflow above an altitude of about 10 km. There is also an inflow at an altitude of around 8 km below the outflow at a radius of 250 km to 500 km. The inflow decreases as it approaches the center of the TC and weakens as it reaches a radius of 250 km. Such a flow from the middle to the lower troposphere is considered MDI (Didlake et al. 2018). The vertical wind field (Fig. 3(c)) shows an updraft at a radius of around 50 km, corresponding to that of the inner eyewall, and an upwelling at radii of around 150 km to 200 km, leading to the formation of the outer eyewall. Outside of that, at a radius from 300 km to 500 km, there is a downdraft in the region corresponding to the inflow in the middle and upper troposphere (Fig. 3(b)). The humidity field (Fig. 3(d)) shows dry air intruded in the middle troposphere in the radius from 500 km up to around 300 km, corresponding to the mid-tropospheric inflow (Fig. 3(b)).

Figure 3(e) shows the agradient wind component, calculated from the output of instantaneous values every 10 minutes and averaged over 3 h. In the middle layer at a radius of 400 km to 500 km at an altitude of 8 km, the negative values are distributed where the inflow exists, consistent with Wang et al. (2020). In the lower layer at a radius

of 150 km to 250 km, as the tangential wind strengthens, a force acts to weaken the inflow due to the off-axis wind component $\bar{v}\left(f+\frac{\bar{v}}{r}\right)-\frac{1}{\rho}\frac{\partial \bar{p}}{\partial r}$, where $^-$ represents an azimuthal mean. This force causes convergence and induces convection outside the original eyewall, leading to SEF outside the inner eyewall. The induction of convection for the secondary eyewall as a result of such boundary layer non-equilibrium dynamics has been suggested by Huang et al. (2012).

3.2 Sensitivity experiments

To investigate the effect of water vapor outside the TC, we conducted the sensitivity experiments qv1.1 and qc1.2, as described in Section 2. The radius-time Hovmöller diagram of precipitation shows SEF in both sensitivity experiments (Fig. 4). However, SEF tends to occur later in these experiments than in CTL, as water vapor outside the TC increases, indicating that this more water vapor condition is unfavorable for SEF. In addition, the precipitation area corresponding to the outer eyewall extends farther outward as water vapor content increases. A similar feature is seen in the radius-time Hovmöller diagram of the surface tangential wind speed (Fig. 4). By contrast, the precipitation and tangential wind speeds at a radius of around 50 km show that the inner eyewall remains strong until a later time, as the water vapor content increases.

4. The mechanism

Next, we analyzed why the water vapor in the mid-upper troposphere outside the TC affects SEF. Here, we compare the results of qv1.2 with those of the control experiment.

The sensitivity of qv1.1 is almost the same as that of qv1.2 shown below. In particular, we show the azimuthally averaged radius-height cross-section at 114 h in the region spanning from the TC center to a radius of 1500 km.

Figure 5(a) shows diabatic heating due to cloud microphysics (shading) and density (contour). The diabatic heating is averaged over 3 h from hourly instantaneous values from 111 h to 114 h. When the water vapor outside the TC increases, the diabatic heating becomes more of a heating anomaly compared to CTL in the domain covering altitudes of 5–8 km and radii of 250–500 km. In this domain, diabatic cooling due to evaporation or sublimation of clouds occurs in the mid-level dry inflow in CTL. When the induced air is more humid, the cooling by evaporation or sublimation becomes weakened. The heating anomaly in diabatic heating causes the air temperature to rise, resulting in a negative density anomaly. Figure 5(b) shows vertical wind (shading) and pressure (contour). The vertical wind becomes more positive in the domain spanning altitudes of 5–8 km and radii 250–500 km, where downdrafts are observed in CTL. This domain corresponds to the positive density anomalies (Fig. 5(a)), which cause weaker downdrafts (i.e., the updraft anomalies) than in CTL, as shown in Fig. 5(b). Figure 5(c) shows the pressure gradient force $-\frac{1}{\rho}\frac{\partial \bar{p}}{\partial r}$ (shading) and the pressure (contour). The pressure gradient force is a 3-h average of instantaneous values every 10 minutes from 111 h to 114 h. In Fig. 5(c), a low-pressure anomaly occurs around an altitude of 5 km below the updraft anomaly, and a high-pressure anomaly occurs around an altitude of 11 km above the updraft anomaly. The pressure gradient force is positive outside of the maximum of the high-pressure anomaly at an altitude of 11 km and radii between 500 and 1000 km. In this domain, the inward pressure gradient force becomes smaller than that in CTL. The

smaller pressure gradient force weakens the mid-level inflow more than in CTL, as shown in Fig. 5(d).

We next examine the angular momentum budget, which is represented by the equation

$$\frac{\partial \bar{M}}{\partial t} = -\bar{u}\frac{\partial \bar{M}}{\partial r} - \overline{u'\frac{\partial M'}{\partial r}} - \bar{w}\frac{\partial \bar{M}}{\partial z} - \overline{w'\frac{\partial M'}{\partial z}} - \overline{\frac{v'}{r}\frac{\partial M'}{\partial \lambda}} - \overline{\frac{1}{\rho}\frac{\partial p'}{\partial \lambda}} + r\bar{F}_v,$$

where t, r, λ, and z represent time, radius, azimuth, and altitude, respectively; u, v, w, ρ, and p represent radial wind, tangential wind, vertical wind, density, and pressure, respectively; $M = rv + \frac{1}{2}fr^2$ denotes angular momentum where f is the Coriolis parameter; and F_v is the tendency due to a turbulent process. $\bar{A}$ represents the azimuthal mean of variable A, and A' represents the deviation from $\bar{A}$. Figure 5(d) shows the inward transport of angular momentum. This is the 3-h average of the instantaneous values every 10 minutes between 111 h and 114 h. The inward transport of angular momentum is smaller than in CTL in the domain around altitudes of 4–8 km and radii 250–400 km, where the inflow becomes weaker than in CTL. This results in tangential winds in the middle and upper troposphere being weaker than in CTL, as shown by Fig. 5(f).

Next, we examine the response in the lower troposphere to the changes in water vapor outside the TC. We show the response at 126 h, which is later than the analysis shown in Fig. 5, when the SEF starts at a radius of around 150 km from the center of the TC. Figure 6(a) shows the sum of Coriolis and centrifugal forces $\bar{v}\left(f + \frac{\bar{v}}{r}\right)$ for the 3-h average of instantaneous values every 10 minutes from 123 h to 126 h. It is negatively distributed in the region comprising radii 100–250 km. The difference in the tangential wind between CTL and qv1.2 (Fig. 6(b)) has almost the same distribution as the sum of Coriolis and

centrifugal forces. When the tangential wind is weaker than in CTL, the sum of the forces acts toward increasing inflow. It increases with decreasing radius and is particularly large at a radius of around 150 km, which is the SEF area in CTL. When the force acts to strengthen the inflow, a divergence anomaly is generated (contours in Fig. 6(c)). Downdraft anomalies also respond to divergence anomalies (shading in Fig. 6(c)). The tangential wind speed increases when the angular momentum transport due to inflow overcomes the frictional deceleration, and the resulting agradient wind component acts to weaken the boundary layer inflow. The increased tangential wind speed leads to convergence in the SEF region and induces convection.

SEF is weakened in these sensitivity experiments in which the amount of water is increased outside the TC, schematically shown in Fig. 7. The upper-level process is related to the change in MDI (Didlake et al. 2018), while the lower-level process is the boundary layer non-equilibrium dynamics (Huang et al. 2012).

5. Conclusions

This study used idealized numerical experiments to investigate the effects of dry air inflow and cooling by evaporation and sublimation in the middle and upper troposphere on SEF. Experiments were conducted using NICAM on an f-plane over a constant sea surface temperature. CTL reproduces SEF and the eyewall replacement cycle. The analysis of CTL reveals dry air inflow in the middle and upper troposphere and the formation of downdrafts due to diabatic cooling. SEF is induced by agradient tangential winds caused by the angular momentum transports due to MDI.

To investigate the proposed mechanism, we conducted two experiments in which the

amount of water vapor in the middle and upper troposphere outside the TC is increased just before SEF. These experiments showed that SEF is delayed and less favorable. In these experiments, evaporation and sublimation cooling in the inflow region weaken, and this change in diabatic cooling leads to updraft anomalies and weaker inflow in the middle of the troposphere, which are associated with lower and higher pressure anomalies below and above the updraft anomaly, respectively, and a smaller inward pressure gradient in the middle troposphere. The tendency due to the angular momentum transport becomes smaller because of the weakening of the inflow, and the tangential wind also weakens.

The weakening of tangential wind in the middle troposphere extends to the lower troposphere. As tangential wind weakens, the agradient wind component acts to strengthen the inflow. The force that strengthens the inflow causes divergence anomalies and weakens convection in the region of SEF.

The present study clarifies the mechanism of SEF using an idealized experiment. We analyzed the numerical results and confirmed that the mechanism involves MDI (Didlake and Houze 2013; Didlake et al. 2018) and the boundary layer non-equilibrium dynamics (Huang et al. 2012). Consequently, we will investigate sensitivities to water vapor outside TCs in realistic cases. Our preliminary results confirm that varying the water vapor in the initial field affects the formation of SEF. The results of the present study indicate that better forecasts of TC structures and intensities require more detailed observations of the water vapor field around TCs.

Acknowledgments

The numerical simulations were conducted using the FUJITSU Supercomputer

PRIMEHPC FX1000 and FUJITSU Server PRIMERGY GX2570 (Wisteria/BDEC-01) at the Information Technology Center, The University of Tokyo. This research was supported by JST Moonshot R&D Grant Number JPMJMS2282 and JSPS Core-to-Core Program, "International Core-to-Core Project on Global Storm Resolving Analysis".

Declaration

The authors have no conflicts of interest to declare.

Author contributions

K. K. and M. S. designed this study. K. K. conducted the simulations and analyzed the data of this study. K. K wrote the manuscript. M. S. edited and both approved the manuscript.

Data Availability Statement

The numerical experimental data are provided by requests to the authors.

Keywords

tropical cyclone, secondary eyewall formation, eyewall replacement cyclone, mesoscale descending inflow

1 **References**

2 Didlake, A. C., P. D. Reasor, R. F. Rogers, and W.-C. Lee, 2018: Dynamics of the
3 transition from spiral rainbands to a secondary eyewall in Hurricane Earl (2010). *J.*
4 *Atmos. Sci.*, **75**, 2909-2929.

5 Didlake, A. C., Jr., and R. A. Houze Jr., 2013: Dynamics of the stratiform sector of a
6 tropical cyclone rainband. J. Atmos. Sci., 70, 1891–1911.

7 Ge, X. Y., 2015: Impacts of environmental humidity on concentric eyewall structure.
8 *Atmos. Sci. Let.*, **16**, 273-278.

9 Huang, Y.-H., M. T. Montgomery, and C.-C. Wu, 2012: Concentric eyewall formation
10 in Typhoon Sinlaku (2008). Part II: Axisymmetric dynamical processes. *J. Atmos.*
11 *Sci.*, **69**, 662-674.

12 Kanada, S., and A. Nishii, 2023: Observed concentric eyewalls of supertyphoon
13 Hinnamnor (2022). SOLA, 19, 70−77, doi:10.2151/sola.2023-010.

14 Kepert, J. D., 2013: How does the boundary layer contribute to eyewall
15 replacement cycles in axisymmetric tropical cyclones? *J. Atmos. Sci.*, **70**, 2808-
16 2829.

17 Nakanishi, M., 2001: Improvement of the Mellor-Yamada turbulence closure model
18 based on large eddy simulation data. *Bound.-Layer Meteor.*, **99**, 349- 378.

19 Nakanishi, M., and H. Niino, 2004: An improved Mellor-Yamada Level-3 model with
20 condensation physics: Its design and verification. *Bound.-Layer Meteor.*, **112**, 1-31.

21 Nakanishi, M., and H. Niino, 2006: An improved Mellor-Yamada Level-3 model: Its
22 numerical stability and application to a regional prediction of advection fog.
23 *Bound.-Layer Meteor.*, **119**, 397-407.

24 Ohno, T., and M. Satoh, 2015: On the warm core of a tropical cyclone formed near
25 the tropopause. *J. Atmos. Sci.*, **72**, 551-571.

26 Roh, W., and M. Satoh, 2014: Evaluation of precipitating hydrometeor
27 parameterizations in a single-moment bulk microphysics scheme for deep
28 convective systems over the tropical central Pacific. *J. Atmos. Sci.*, **71**, 2654-2673.

29 Rotunno, R., and K. A. Emanuel, 1987: An air-sea interaction theory for tropical
30 cyclones. Part II: Evolutionary study using a nonhydrostatic axisymmetric
31 numerical model. *J. Atmos. Sci*, **44**, 542-561.

Satoh, M., T. Matsuno, H. Tomita, H. Miura, T. Nasuno, and S. Iga, 2008: Nonhydrostatic Icosahedral Atmospheric Model (NICAM) for global cloud resolving simulations. *J. Computational Phys.*, **227**, 3486-3514.

Satoh, M., Tomita, H., Yashiro, H., Miura, H., Kodama, C., Seiki, T., Noda, A. T., Yamada, Y., Goto, D., Sawada, M., Miyoshi, T., Niwa, Y., Hara, M., Ohno, T., Iga, S., Arakawa, T., Inoue, T., Kubokawa, H., 2014: The Non-hydrostatic Icosahedral Atmospheric Model: Description and Development. Progress in Earth and Planetary Science, 1, 18, doi:10.1186/s40645-014-0018-1.

Terwey, W. D., and M. T. Montgomery, 2008: Secondary eyewall formation in two idealized, full-physics modeled hurricanes. *J. Geophys. Res.*, **113**, D12112.

Tomita, H., 2008: New microphysical schemes with five and six categories by diagnostic generation of cloud ice. *J. Meteor. Soc. Japan*, **86**, 121-142.

Tomita, H. and Satoh, M., 2004 : A new dynamical framework of nonhydrostatic global model using the icosahedral grid. Fluid Dyn. Res., 34, 357-400, DOI:10.1016/j.fluiddyn.2004.03.003.

Wang, H., Y. Wang, J. Xu, and Y. Duan, 2019: The axisymmetric and asymmetric aspects of the secondary eyewall formation in a numerically simulated tropical cyclone under idealized conditions on an f plane. *J. Atmos. Sci.*, **76**, 357-378.

Wang, S., R. K. Smith, and M. T. Montgomery, 2020: Upper-tropospheric inflow layers in tropical cyclones. *Quart. J. Roy. Meteor. Soc.*, **146**, 3466-3487.

Zhu, Z., and P. Zhu, 2014: The role of outer rainband convection in governing the eyewall replacement cycle in numerical simulations of tropical cyclones. *J. Geophys. Res. Atmos.*, **119**, 8049-8072.

List of Figure Captions

Figure 1. Distribution of 1-h accumulated precipitation [mm] at (a) 114 h, (b) 120 h, (c) 126 h, (d) 132 h, (e) 138 h, and (f) 144 h.

Figure 2. Radius-time cross-section of azimuthally averaged precipitation [mm] (a) and tangential surface wind [m s^{-1}] (b). Time series of maximum tangential wind (red

line) and radius of maximum tangential wind (blue line) at surface (c).

Figure 3. Radius-height cross-section of azimuthally averaged (a) tangential wind [m s^{-1}], (b) radial wind [m s^{-1}], (c) vertical wind [m s^{-1}], (d) relative humidity, and (c) agradient force [m s^{-1} h^{-1}].

Figure 4. Radius-time cross-section of azimuthally averaged (top) precipitation [mm] and (bottom) tangential surface wind [m s^{-1}]. (a) and (d), CTL; (b) and (e), the qv1.1 experiment; and (c) and (f), the qv1.2 experiment.

Figure 5. Difference between CTL and qv1.2 in the axisymmetric radius-height cross-section at 114 h (qv1.2 – CTL). (a) diabatic heating rate [K h^{-1}] (3-h average every 1 h) and density [g m^{-3}], (b) vertical wind [m s^{-1}] and pressure [Pa], (c) mean horizontal transport of angular momentum budget [10^5 m^2 s^{-1} h^{-1}] (3-h average every 10 minutes), (d) radial wind [m s^{-1}], (e) pressure [Pa] and pressure gradient force [m s^{-1} h^{-1}] (3-h average every 10 minutes), and (f) tangential wind [m s^{-1}].

Figure 6. The same as Fig. 5 but for (a) the sum of Coriolis force and centrifugal force $\bar{v}\left(f+\frac{\bar{v}}{r}\right)$ [m s^{-1} h^{-1}], (b) tangential wind [m s^{-1}], and (c) vertical wind [m s^{-1}] and the divergence [s^{-1}].

Figure 7. Schematic diagrams of the response of the sensitivity experiment in which the amount of water vapor outside the TC is increased: (a) the upper-level process and (b) the lower-level process. In (a), the reduced evaporation or sublimation of water

vapor reduces the downward motion of MDI (1), which is associated with the high- and low-pressure responses above and below the upward response region, respectively, (2), and then the mid-level inflow is reduced (3). The reduced MDI leads to the weakening of tangential wind in the region indicated by (4) (and (1) in (b)). In (b), the smaller tangential wind speed (1) enhances the lower inflow at the bottom of MDI (2) and reduces the convergence in the outer eyewall region (3).

Figure 1. Distribution of 1-h accumulated precipitation [mm] at (a) 114 h, (b) 120 h, (c) 126 h, (d) 132 h, (e) 138 h, and (f) 144 h.

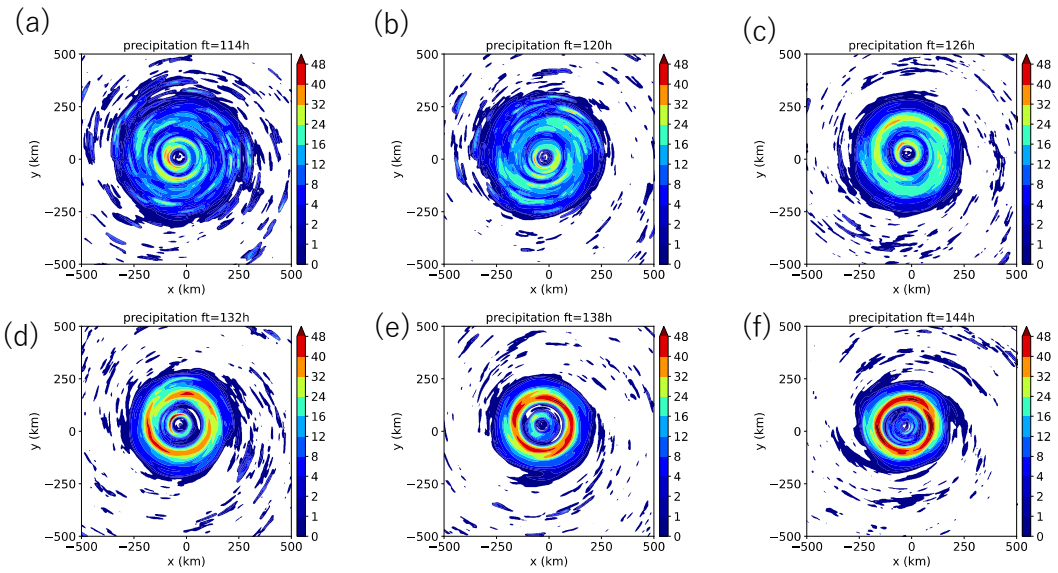

Figure 2. Radius-time cross-section of azimuthally averaged precipitation [mm] (a) and tangential surface wind [m s^{-1}] (b). Time series of maximum tangential wind (red line) and radius of maximum tangential wind (blue line) at surface (c).

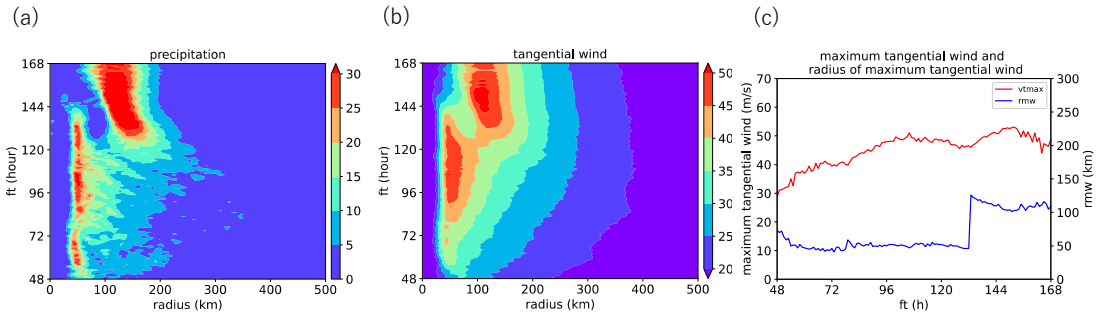

Figure 3. Radius-height cross-section of azimuthally averaged (a) tangential wind [m s^{-1}], (b) radial wind [m s^{-1}], (c) vertical wind [m s^{-1}], (d) relative humidity, and (c) agradient force [m s^{-1} h^{-1}].

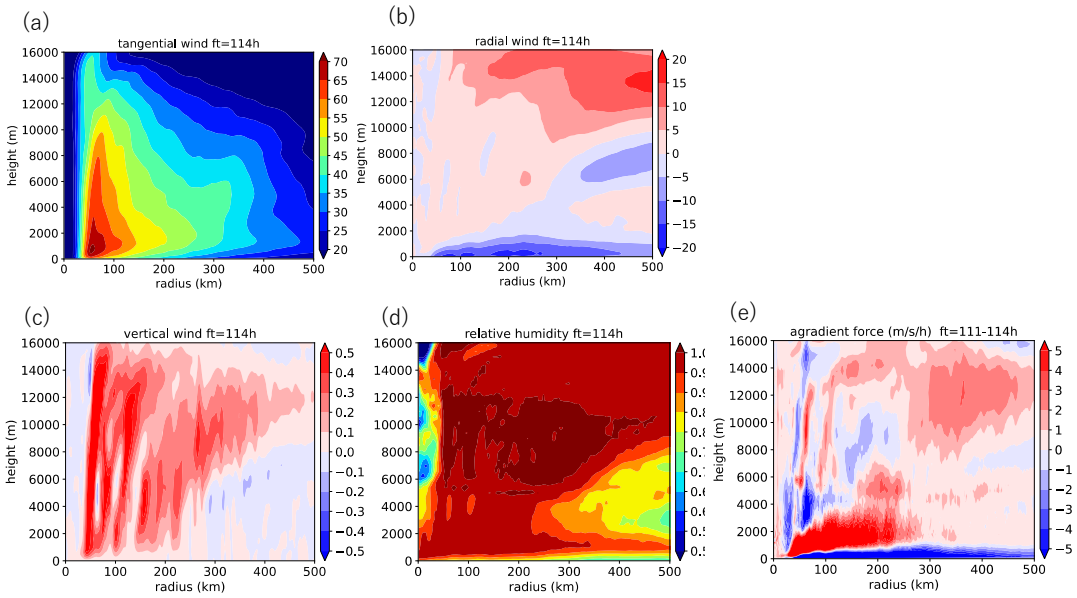

Figure 4. Radius-time cross-section of azimuthally averaged (top) precipitation [mm] and (bottom) tangential surface wind [m s^{-1}]. (a) and (d), CTL; (b) and (e), the qv1.1 experiment; and (c) and (f), the qv1.2 experiment.

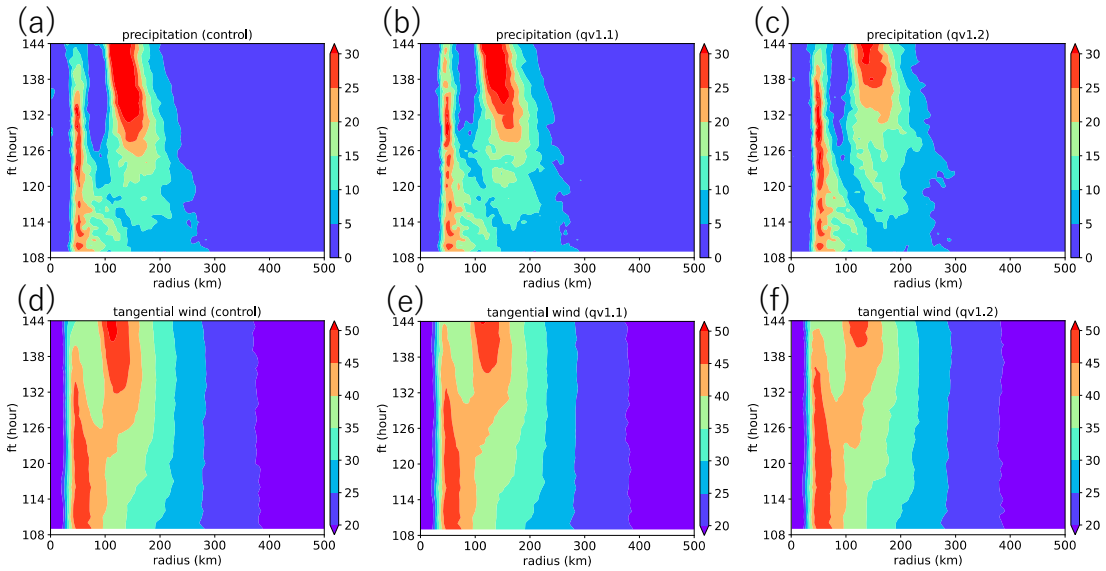

Figure 5. Difference between CTL and qv1.2 in the axisymmetric radius-height cross-section at 114 h (qv1.2 – CTL). (a) diabatic heating rate [K h^{-1}] (3-h average every 1 h) and density [g m^{-3}], (b) vertical wind [m s^{-1}] and pressure [Pa], (c) mean horizontal transport of angular momentum budget [10^5 m^2 s^{-1} h^{-1}] (3-h average every 10 minutes), (d) radial wind [m s^{-1}], (e) pressure [Pa] and pressure gradient force [m s^{-1} h^{-1}] (3-h average every 10 minutes), and (f) tangential wind [m s^{-1}].

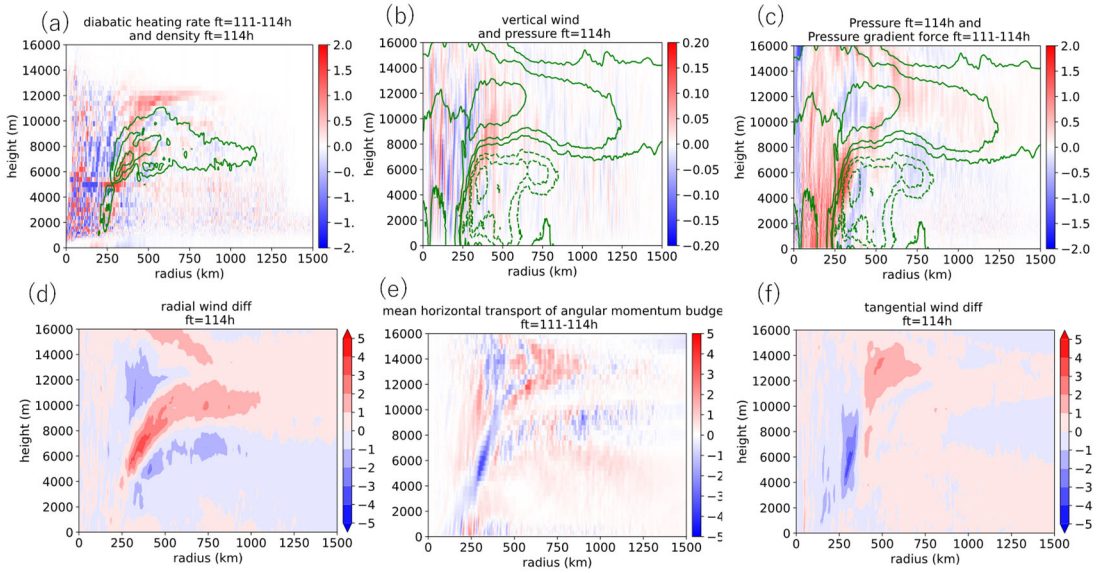

Figure 6. The same as Fig. 5 but for (a) the sum of Coriolis force and centrifugal force $\bar{v}\left(f+\frac{\bar{v}}{r}\right)$ [m s^{-1} h^{-1}], (b) tangential wind [m s^{-1}], and (c) vertical wind [m s^{-1}] and the divergence [s^{-1}].

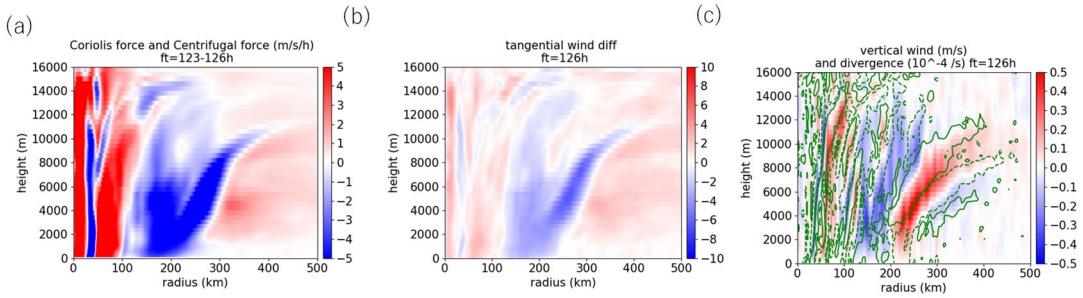

Figure 7. Schematic diagrams of the response of the sensitivity experiment in which the amount of water vapor outside the TC is increased: (a) the upper-level process and (b) the lower-level process. In (a), the reduced evaporation or sublimation of water vapor reduces the downward motion of MDI (1), which is associated with the high- and low-pressure responses above and below the upward response region, respectively, (2), and then the mid-level inflow is reduced (3). The reduced MDI leads to the weakening of tangential wind in the region indicated by (4) (and (1) in (b)). In (b), the smaller tangential wind speed (1) enhances the lower inflow at the bottom of MDI (2) and reduces the convergence in the outer eyewall region (3).